Large eddy simulation of boundary-layer turbulence over the heterogeneous surface in the Source Region of the Yellow River

Yunshuai ZHANG[1], Qian HUANG[1,*], Yaoming MA[1,2,3,4], Jiali LUO[1], Chan WANG[5], Zhaoguo LI[5], and Yan CHOU[1]

[1] *Key Laboratory for Semi-Arid Climate Change of the Ministry of Education, College of Atmospheric Sciences, Lanzhou University, Lanzhou 730000, China*

[2] *Land-Atmosphere Interaction and its Climatic Effects Group, State Key Laboratory of Tibetan Plateau Earth System, Resources and Environment (TPESRE), Institute of Tibetan Plateau Research, Chinese Academy of Sciences, Beijing 100101, China.*

[3] *University of Chinese Academy of Sciences, Beijing 100049, China*

[4] *CAS Center for Excellence in Tibetan Plateau Earth Sciences, Chinese Academy of Sciences, Beijing 100101, China*

[5] *Key Laboratory of Land Surface Process and Climate Change in Cold and Arid Regions, Northwest Institute of Eco-Environment and Resources, Chinese Academy of Sciences, Lanzhou 730000, China*

Abstract

Lake breezes are proved by downdrafts and the divergence flows of zonal wind in the source region of the Yellow River (SRYR) in the daytime based on ERA-Interim reanalysis data. In order to depict the effect of the circulations induced by surface anomaly heating (patches) on the boundary-layer turbulence, the large eddy model was used to produce a set of 1D strip-like surface heat flux distributions based on observations, which obtained by a field campaign in the Ngoring Lake Basin in the summer of 2012. The simulations show that for the cases without background wind, patch-induced circulations (SCs) promote the growth of convective boundary layer (CBL), enhance the turbulent kinetic energy (TKE) and then modify the spatial

---

*Corresponding author.
E-mail address: huangq@lzu.edu.cn (Q. Huang).

distribution of TKE. Based on phase-averaged analysis, which separates the attribution from the SCs and the background turbulence, the SCs contribute no more than 10% to the vertical turbulent intensity, but their contributions to the heat flux can be up to 80%. The thermal internal boundary layer (TIBL) reduce the wind speed and form the stable stratification, produce the obvious change of turbulent momentum flux and heat flux over the heterogeneous surfaces. The increased downdrafts, which mainly occur over the lake patches and carry more warm, dry air down from the free atmosphere. The background wind inhibits the SCs and the development of the CBL, it also weakens the patch-induced turbulent intensity, heat flux, and convective intensity.

Key word: turbulence, heat flux, heterogeneously surface heating, background wind, phase-averaged analysis

1. Introduction

Turbulence in the planetary boundary layer (PBL), which is derived from surface heating and surface fraction, plays an important role in the exchange of heat, momentum, moisture, and chemical constituents between the surface and free atmosphere (Zhang et al., 2018). Previous studies on the turbulence and turbulent exchange over homogeneous surfaces based on Monin-Obukhov similarity theory were conducted before the 1990s (Sommeria and LeMone, 1978; Moeng, 1984). Then turbulence over heterogeneous surfaces was investigated through field campaigns (Wang et al., 2016; Zhao et al., 2018) and numerical simulations (Shao et al., 2013; Liu et al., 2011) in the past few decades, which help us better understand the

49   interactions between the surface and atmosphere. Thermal surface heterogeneity is a

50   typical issue and leads to the formation of local/secondary circulations. Sea and lake

51   breezes are a well-known example of flows that are generated by heterogeneous

52   surface heating between the land and water (Crosman and Horel, 2012). Observations

53   have also revealed the imbalance in the surface energy budget over heterogeneous

54   surfaces (Foken et al. 2010; Xu et al., 2016). The most widely used eddy covariance

55   (EC) system for a single site has been shown to underestimate the turbulent flux due

56   to the large-eddy transport or secondary circulations not being captured (Foken et al.,

57   2010; Xu et al., 2016). The simulation studies conducted by Zhou et al. (2018) and

58   Frederik and Matthias (2018) showed that the flux induced by mesoscale or secondary

59   circulations is the main reason for the energy imbalance. Moreover, the PBL

60   parameterization schemes in the weather/climate model over a heterogeneous surface

61   have been continuously improved until now (Avissar and Pielke, 1989; Shao et al.,

62   2013). Different surface patterns such as mosaic (Avissar and Schmidt, 1998),

63   chessboard (Liu et al., 2011; Shen et al., 2016), patchy-like (Zhou et al., 2018), and

64   strip-like (Li et al., 2011; Wang et al., 2011) patterns have been utilized to simulate

65   thermodynamic surface heterogeneity. These studies confirmed that the secondary

66   circulation induced by the surface heterogeneity influences the PBL's properties and

67   turbulent characteristics. In addition, several studies have examined the effects of

68   surface heterogeneity on different levels of background wind (Shen and Leclerc, 1995;

69   Liu et al., 2020) and the direction relative to the orientation of the heterogeneity

70   (Wang et al., 2011; Kang and Lenschow, 2014), as well as the spatial and temporal

71 variations of the wind fields (Liu et al., 2018). However, the issues related to the

72 effects of the surface heterogeneity in special areas still need to be explored.

73   The dynamic and thermodynamic influences of the Tibetan Plateau (TP) on the

74 regional and global weather and climate systems are closely related to its PBL, and

75 turbulence plays a significant role in the mass and energy exchange between the TP

76 and the atmosphere (Chen et al., 2013; Chen et al., 2016). Different landscapes make

77 up the heterogeneous land surface over the TP. As the Asian Water Tower, lakes are

78 widely and densely distributed over the TP, which affects the overlying energy and

79 mass transport through the lake-air turbulent heat flux. Biermann et al. (2014) and

80 Wang et al. (2015) discovered that the turbulent flux of Lake Nam co, which is

81 surrounded by wet grasslands, is actually very considerable but was often

82 underestimated by a hydrodynamic multilayer model from Foken (1979 and 1984).

83 The Source Region of the Yellow River (SRYR) is located in the northeastern part of

84 the TP and is known as the "water tower" of China because it contains 48 lakes. The

85 Ngoring and Gyaring (Sisters) Lakes are two major lakes, and Ngoring Lake is the

86 largest in the SRYR (Li et al., 2015; Wen et al., 2015). In addition to the lakes, the

87 forests, alpine meadow, wetlands, rivers, and glaciers comprise the diverse underlying

88 surfaces in the SRYR, with grassland accounting for about 80% of the area (Mudassar

89 et al., 2018). Consequently, the SRYR is an ideal region for studying the turbulence

90 over a heterogeneous land surface.

91   Observational studies have revealed that water vapor, heat and energy exchange

92 occur over alpine meadows/wetlands (Zheng et al., 2015; Jia et al., 2017) and lakes

93   (Li et al., 2015; Wen et al., 2016), and models have been used to simulated the effects

94   of the lakes on the cool and moist regional climate (Wen et al., 2015; Ao et al., 2018).

95   However, the features of the boundary-layer turbulence over the heterogeneous

96   underlying surfaces and the effects of thermodynamic surface heterogeneity on the

97   turbulent flux in the SRYR remain unclear. Over the last few decades, the lakes have

98   shrunk and the grasslands have degraded in the SRYR due to climate change and the

99   excessive utilization of water resources (Brierley et al., 2016; Mudassar et al., 2018).

100   It is essential to investigate the variation in the structure of boundary-layer and

101   turbulent heat flux with changes in the surface's thermal properties and the

102   background wind.

103   High resolution field measurements are extremely rare on the TP because of the

104   harsh environmental conditions, so few observational studies on the turbulence

105   characteristics and the turbulent heat flux have been conducted. Large eddy

106   simulation (LES) has the unique advantage of being accurate and able to describe

107   turbulence finely, and thus, it has been widely used to investigate the effects of

108   surface heterogeneity on turbulence (Hadfield et al., 1991, 1992; Kang and Lenschow,

109   2014). However, little has been done to improve our understanding of how the surface

110   heterogeneity affects the boundary-layer turbulence, and the contributions of the

111   patch-induced motions to the turbulent flux and energy in the SRYR. Furthermore,

112   modeling the turbulence over the heterogeneous surface in the SRYR can not only lay

113   a basis for the analysis of the local energy and mass transport, but it can also provide a

114   quantitative   reference   for   improving   the   parameterization   schemes   over

115   heterogeneous surfaces in weather and climate models.

116   In this study, we used LES to investigate the detailed turbulence characteristics in

117   the SRYR. Our primary focus was the impacts of the surface heat flux anomalies on

118   the turbulent kinetic energy (TKE), turbulent intensity, and turbulent flux. The

119   turbulence characteristics and turbulent fluxes in the surface and the entrainment

120   layers of PBL were investigated, too. This paper is arranged as follows Section 2

121   describes the model and data used in this study. Section 3 discusses the modeled

122   results in detail, and section 4 provides a summary and discussion of our findings.

123   ## 2   Data and methods

124   ### 2.1   Study area and observations

125   Ngoring Lake and Gyaring Lake (hereinafter referred to as the two lakes) are

126   located in the SRYR and are surrounded by the alpine meadow. Their mean elevation

127   is 4274 m above sea level. The study area is shown in Fig. 1. The turbulent flux and

128   standard atmospheric variables were measured over the lake and grassland surface.

129   The GPS radiosonde data from the field campaign on July 29, 2012, at 30 m west of

130   Lake Ngoring (near the gradient tower station, TS) and Madoi station (MD) located

131   30 km the east of the lake (34.918° N, 98.216° E, 4279 m AMSL). The eddy

132   covariance data for Lake Station (LS) above the northwest of the lake (35.026° N,

133   97.652° E) and Grassland Station (GS) (34.913° N, 97.553° E) at 1.5 km west of the

134   lake shore were used. For further details on the field campaign and the quality control

135   of the sounding and eddy covariance data, see Li et al. (2015) and Li et al. (2017).

136   The synoptic background at 500 hPa and the distribution of the wind components in

the vertical and horizontal directions were investigated using the ERA-Interim

Reanalysis Data with a 0.25° × 0.25° resolution collected at 12:30 LT and 18:30 LT

(LT: local time, used in the whole study) on July 29, 2012, with a delimiting a range

of 32° N–37° N, 95° E–100° E, including the two lakes area (34.8° N–35° N, 97°

E–98° E) and the surrounding grassland.

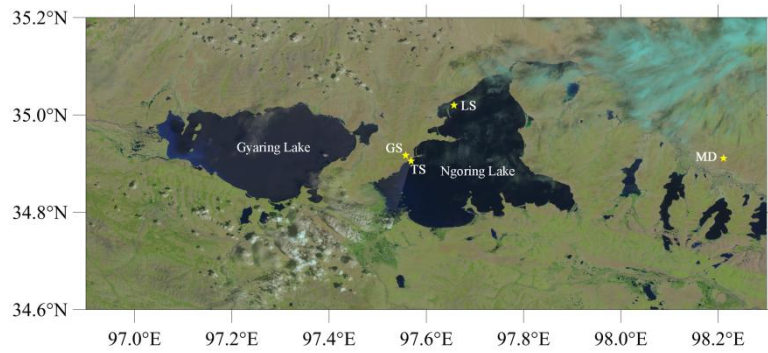**Figure 1.** Map of the study area obtained using Landsat data on 21th August, 2014, with the location of the observation stations marked by yellow stars. The turbulent fluxes were measured at LS and GS stations. The standard atmospheric variables were observed at the TS. MD is a fixed meteorological observatory of the China Meteorological Administration.

2.2   Methods

2.2.1   Simulations set-up over the heterogeneous underlying surface

The U.K. Met Office large eddy model (LEM) version 2.4 (Gray et al., 2001) was

used in this paper. The LEM is a three-dimensional and non-hydrostatic numerical

model, which can be used to simulate a wide range of turbulence-scale and

cloud-scale problems with a high resolution. The domain size was 135 km×30 km×

6 km in the y, x and z direction respectively, with a horizontal grid-spacing of 200 m.

According to Honnert et al. (2011) and Honnert et al. (2020), the horizontal resolution

of 200 m is reasonable in this LEM study. There were 74 levels in the vertical

direction, with a vertically stretched grid having a minimum spacing of 1.1 m in the

156 surface layer and a maximum of 64.8 m above 2000 m. Periodic lateral boundary

157 conditions were applied, with a rigid lid at the top of the model domain. To reduce the

158 reflection of the internal gravity waves, a Newtonian damping layer was applied

159 above 3500 m. The surface boundary conditions of the model were derived from the

160 Monin-Obukhov similarity theory using the Businger-Dyer functions. The subgrid

161 model used in the LEM was based on the Smagorinsky-Lilly approach (Brown et al.,

162 1994). The potential temperature, wind (u and v), and relative humidity profiles

163 obtained during the field campaign on July 29, 2012, were used to initialize the 3D

164 runs. The LEM was driven by the time-varying sensible heat flux (SHF) and the latent

165 heat flux (LHF) at the surface. The geostrophic wind shear was calculated using the

166 ERA-Interim geostrophic wind at the surface and at 1500 m. These conditions will be

167 detailed on Fig. 2. The simulation time was 12 hours and the data were output every

168 hour. The time step is 0.01s for all simulations. In this study, twelve 3D runs with

169 different surface heat flux under various background wind conditions were performed.

170 Two of the runs were horizontally homogeneous with a uniform grass surface under

171 the conditions of wind (HOMW) and no wind (HOM). The other cases were

172 simulated with one (A1L) or two (A2L) lake patches in the middle of the model

173 domain. The surface heat flux anomaly was applied over a 30 km wide strip (two

174 strips for A2L) extending the entire 30 km width of the domain in the x-direction.

175 Here the term heat flux refers to both the sensible and latent heat fluxes. This can be

176 viewed as representing Ngoring Lake and Gyaring Lake in the SRYR. It should be

177 noted that in this study the scale of the heterogeneity was large enough to enable the

178 formation of small eddies over the lake patches that could coexist with the large-scale

179 patch-induced circulations (Patton et al., 2005). Four simulations (A1L, A2L, A1LW,

180 and A2LW) were initialized using the surface heat flux over the patch/patches

181 measured at LS and the heat flux outside the patch/patches measured at GS. This

182 means that the heat flux into the modeled atmosphere decreases as the number of

183 patches increases. However, it is helpful to separate the effects of the total increase in

184 heating from the effects of the localization of the heating when considering the

185 consequences of an unresolved spatially changing heat flux for a global model. In

186 order to keep the total heat flux in the modeled atmosphere constant, a "balanced"

187 surface heat flux approach was used. Therefore, if the surface heat flux observed at

188 the GS is denoted as FGS, and the heat flux over the patch and outside of the patch

189 are denoted as FL and FG, respectively. FL and FG were calculated using the

190 following equations:

191 $$FL = FGS \times (SL/ST) \tag{1}$$

192 $$FG = FGS \times (SG/ST) \tag{2}$$

193 where ST, SL, and SG are the squares of the model domain, the patch, and the outside

194 of it, respectively. Another four simulations (A1LC, A2LC, A1LWC, and A2LWC)

195 were performed using this balanced surface heat flux approach. The heterogeneous

196 initial conditions were used in the surface heat flux anomaly simulations. The initial

197 profiles over the patch/patches were derived using the data from TS station, and the

198 data observed at the MD station used for the outside patch/patches. Various

199 background wind conditions were also used for the surface heat flux anomaly runs.

200　The parameters and the conditions of each run are listed in Table 1 for convenience.

201　Sketches of the heterogeneous surface and of the surface heat flux over the lake

202　patches and the outside patches for the unbalanced and balanced cases are depicted in

203　Fig. 2.

204　　The initial potential temperature and special humidity are shown in Fig. 2h, and the

205　horizontal components of the wind profiles and the geostrophic wind are shown in Fig.

206　2g. A stable layer was found over the grass and a 200 m convective boundary layer

207　(CBL) was found over the lake at 06:30 LT. The special humidity profiles show that

208　the air tends to be moister over the lake (dash lines in Fig. 2h). The study area is

209　characterized by a considerable surface heat flux and high wind speeds in the daytime.

210　The stronger initial velocity is from the GS, which recorded wind speeds of up to 10

211　m·s^{-1} below 500 m.

212　**Table 1**

213　Parameters for the 3D simulations over the homogeneous surface (HOM) and

214　heterogeneous surface with surface heat flux anomalies (A) under different conditions:

215　with one (1L) or two (2L) lake patches, with initial wind and geostrophic wind (W),

216　without geostrophic wind (NG), with the constant surface heat flux (C).

Name	Wind field	Surface heat flux (SHF and LHF)	Number of lake patches	Size of Lake patch (km)
HOM	without wind	FGS	0	-
HOMW	initial wind + geostrophic wind	FGS	0	-

|				
A1L	without wind	lake patch: FLS (Heat flux that observed at LS); outside patch: FGS	1	30
A2L	without wind	lake patches: FLS (Heat flux that observed at LS); outside patches: FGS	2	30 and 30
A1LW	initial wind + geostrophic wind	Same as A1L	1	30
A2LW	initial wind + geostrophic wind	Same as A2L	2	30 and 30
A1LNG	initial wind	Same as A1L	1	30
A2LNG	initial wind	Same as A2L	2	30 and 30
A1LC	without wind	lake patch: $(SL/ST) \times FGS = (30/135) \times FGS$; outside patch: $(SG/ST) \times FGS = (105/135) \times FGS$	1	30
A2LC	without wind	lake patches: $(SL/ST) \times FGS = (30/135) \times FGS$; outside patches: $(SG/ST) \times FGS = (75/135) \times FGS$	2	30 and 30
A1LWC	initial wind + geostrophic wind	Same as A1LC	1	30
A2LWC	initial wind + geostrophic wind	Same as A2LC	2	30 and 30
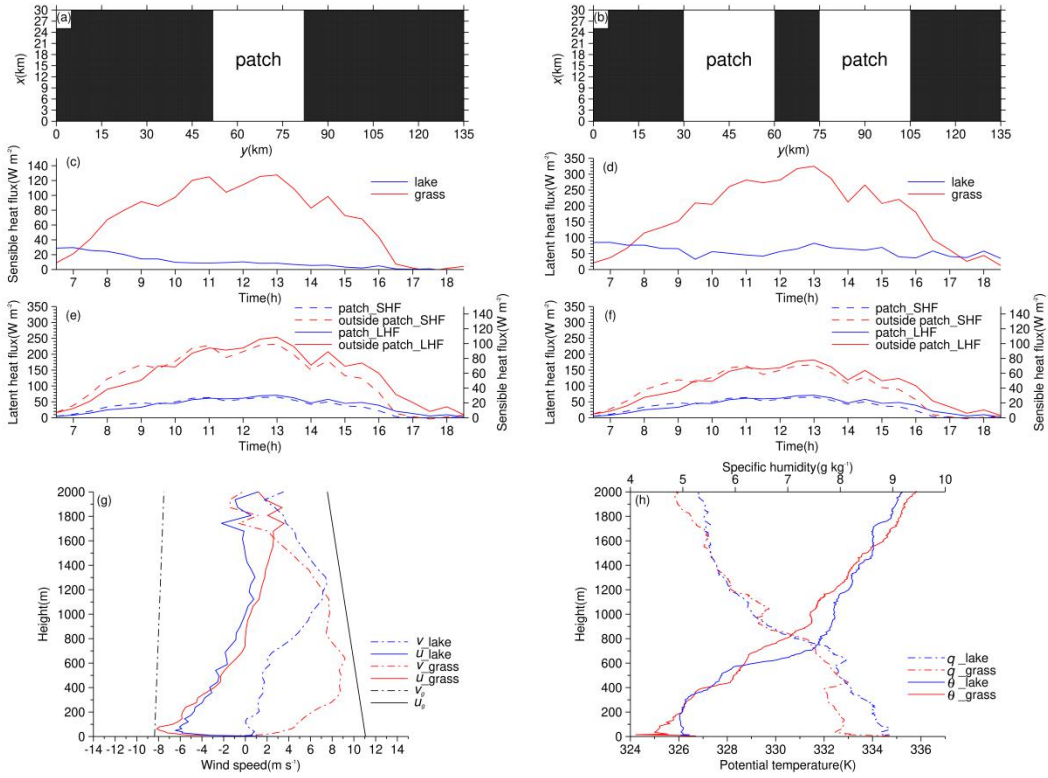
Figure 2. Sketch of the heterogeneous surface (a and b), surface sensible heat flux and latent heat flux (c and d) over the grassland (red line) and the lake (blue line) from observation. The SHF and the LHF for runs with (e) one and (f) two lake patches and a constant heat flux. Figs. 2g and 2h show the model initial profiles of the winds (solid lines for *u*, dash lines for *v*), potential temperature (solid lines), and special humidity (dash lines) over the lake patches (blue lines) and outside of the patches (red lines). The input geostrophic winds are also shown (black lines).

2.2.2 statistical analysis

According to turbulence theory, a physical quantity ϕ has two parts, i.e., the horizontal average $\langle \phi \rangle$ and the turbulent fluctuation ϕ', so

$$\phi = \langle \phi \rangle + \phi' \tag{3}$$

This equation usually works in cases with a homogeneous surface. The variances of velocity and the potential temperature variances ($\sigma_v^2, \sigma_w^2, \sigma_\theta^2$) are calculated from v', w', and θ', respectively. For a heterogeneous surface, phase-averaged analysis helps separate the patch-induced circulations from the random turbulent motions. This

232 method has been applied in studies of the one-dimension and two-dimension

233 heterogeneities (Matthias et al., 2014; Kang and Lenschow, 2014; Shen et al., 2016),

234 as well as the complex and irregular heterogeneities (Maronga and Raasch, 2013). In

235 this study, one-dimensional heterogeneous (in the y direction) simulations were

236 performed for which ϕ can be decomposed into three parts:

237 $\quad \phi = \langle \phi \rangle + \phi_{hi} + \phi_s$ $\hfill$ (4)

238 Where $\langle \phi \rangle$ is the horizontal average; ϕ_{hi} is the heterogeneity-induced part which is

239 the averaged ϕ across the domain in the y direction; and ϕ_s is from the background

240 turbulence. The variances of velocity and the potential temperature induced by the

241 heterogeneity ($\left[\sigma_v^2\right]_{hi}$, $\left[\sigma_w^2\right]_{hi}$, $\left[\sigma_\theta^2\right]_{hi}$) are calculated from v_{hi} , w_{hi} , and θ_{hi} ,

242 respectively.

243 $\quad$ Phase-averaged analysis was also used to obtain the patch-induced component of

244 the turbulent fluxes. We multiplied w and ϕ with both in the forms of Equation (4),

245 and derived the total vertical transport of ϕ :

246 $\quad \overline{\langle w\phi \rangle} = \overline{\langle w \rangle \langle \phi \rangle} + \langle w_{hi} \phi_{hi} \rangle + \overline{\langle w_s \phi_s \rangle}$ $\hfill$ (5)

247 Since the horizontal average vertical velocity $\langle w \rangle$ is approximately zero in the LES,

248 the turbulent fluxes were divided into two parts: circulations induced part and

249 background turbulence induced part:

250 $\quad \overline{\langle w\phi \rangle} = \langle w_{hi} \phi_{hi} \rangle + \overline{\langle w_s \phi_s \rangle}$ $\hfill$ (6)

251 Moreover, the total kinetic energy e can be written as two parts, e_{hi} and e_s , which

252 represent the contributions from the patch-induced and background turbulence:

253 $\quad e = e_{hi} + e_s$ $\hfill$ (7)

254 $$e_{hi} = \left(\left\langle u_{hi}{}^2 \right\rangle + \left\langle v_{hi}{}^2 \right\rangle + \left\langle w_{hi}{}^2 \right\rangle \right) / 2 \qquad (8)$$

255 $$e_s = \left(\left\langle u_s{}^2 \right\rangle + \left\langle v_s{}^2 \right\rangle + \left\langle w_s{}^2 \right\rangle \right) / 2 \qquad (9)$$

256 **3. Results**

257 **3.1. Synoptic background and wind components' distributions**

258   In order to investigate the existence of a daytime (6:30-18:30 LT) lake breeze (the

259 divergent flows over the lake surface and the downdrafts overlying it) using the

260 ERA-Interim reanalysis data with a 0.25° × 0.25° resolution for the two lakes area

261 (34.8° N–35° N, 97° E–98° E; blue box in Fig. 3), the wind field, temperature field,

262 and geopotential height field at 500 hPa (~5500 m) at 12:30 LT and 18:30 LT on July

263 29, 2012 were analyzed. The southerly wind controlled the entire region at 500 hPa at

264 12:30 LT (Fig. 3a) then it became divergent flow at 18:30 LT (Fig. 3b). The vertical

265 sections of the two wind components (u and w) were also depicted to further ascertain

266 the distribution of the wind field in the longitude and latitude directions. It should be

267 noted that downdrafts are dominant below 500 hPa in the two lakes area during the

268 day (Figs. 3c and 3d). As can be seen from Fig. 3f, distinct divergent zonal wind (u)

269 flows existed in the two lakes area at 18:30 LT. The wind speed derived from the GPS

270 sounding at 12:30 LT is larger than that at 18:30 LT below 2 km (see Fig. S1 in

271 supplement), indicating that the larger background wind covered up the divergent

272 wind at 12:30 LT. Evidently, it is difficult to directly observe the lake breeze

273 circulation due to the synoptic background, but the downdrafts and the divergent

274 zonal wind in the two lakes area demonstrate the existence of a lake breeze. In the

275 following sections, the turbulence characteristics over the heterogeneous underlying

276   surface are simulated and the effects of the patch-induced circulation are analyzed.
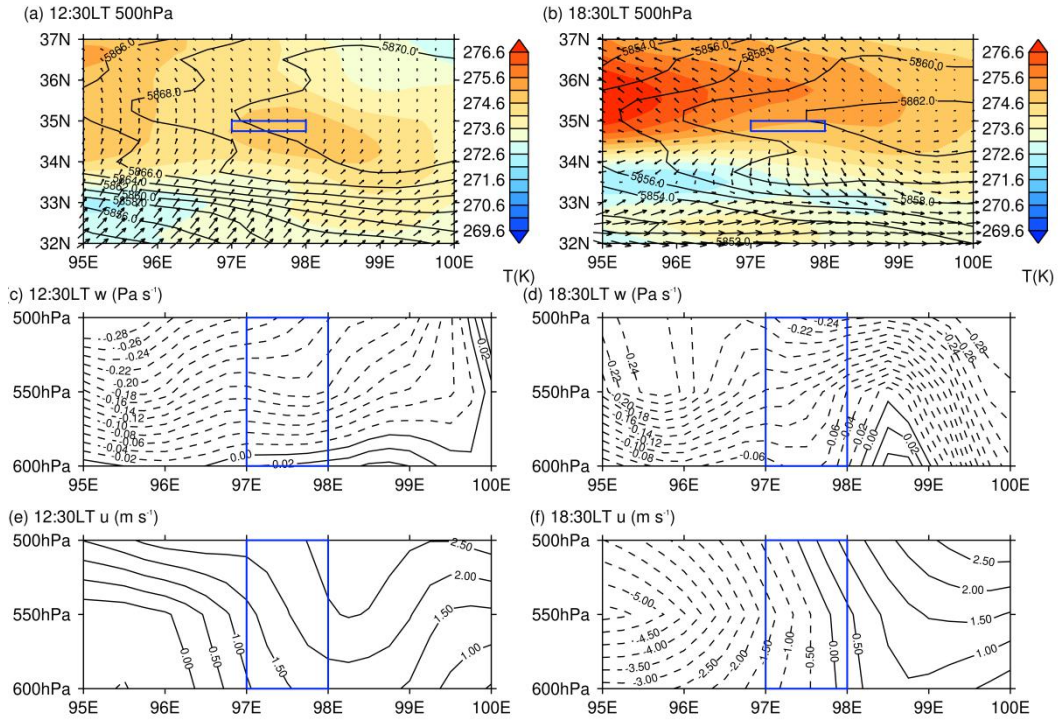
277   **Figure 3.** Synoptic background on July 29, 2012. Blue boxes represent the two lakes area. (a) and
278   (b) show the wind field, temperature field, and geopotential height field at 500 hPa (~5500 m) at
279   12:30 LT (Fig. 3a) and at 18:30 LT (Fig. 3b). The vertical wind (w, Figs. 3c and 3d) and the zonal
280   wind (u, Figs. 3e and 3f) below 500 hPa are also shown.

281   ## 3.2 Effects of the underlying surfaces and background wind on the
282   boundary-layer turbulence

283   ### 3.2.1 Performance of the LEM and the height of the boundary layer over
284   homogeneous and heterogeneous surfaces

285   In order to inspect the performance of the LEM over the heterogeneously heated
286   surfaces, the simulated virtual potential temperature (θ_v) over the lake patch/patches
287   and outside were compared with the observations. In addition, by keeping the total
288   surface heat flux into the modeled domain constant, the profiles of the simulated
289   virtual potential temperature over the homogeneous and heterogeneous surfaces were

290 compared in order to investigate the effects of surface heterogeneity on the structure

291 of the boundary layer. The profiles of the kinematic heat flux for all of the runs were

292 used to determine the height of the boundary layer. Figures 4a and 4b compare the

293 simulated profiles of the virtual potential temperature over and outside of the lake

294 patch with the corresponding observations (solid lines) over the grassland and the lake

295 surfaces at different times. In order to account for the effects of the unrepresented

296 large-scale forcing, the simulated horizontally averaged potential temperature, water

297 vapor mixing ratio, and horizontal wind (u and v) were relaxed to those observed

298 using the radiosondes with a 3 h (hour) interval during the simulation (Marsham et al.,

299 2008; Huang et al., 2009). The time series of the kinetic energy (see Fig. S2 in

300 supplement) indicates that the equilibration time of the model is approximately 3

301 hours.
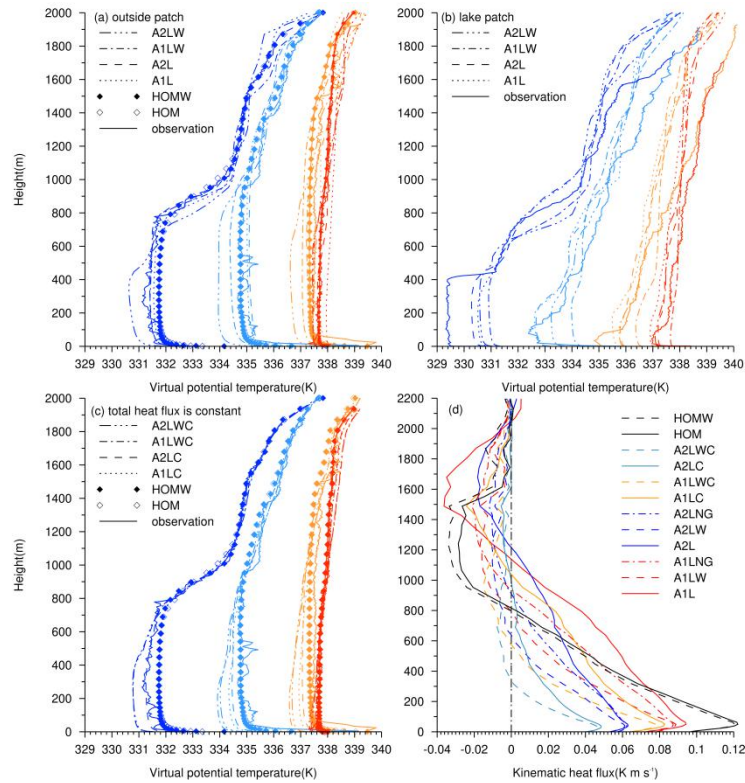
302 **Figure 4.** The profile of the horizontal, averaged virtual potential temperature for the observations

303　and all of the runs over the lake patches (a) and outside of the lake patches (b). (c) same as (a)

304　except, for heterogeneous and homogeneous runs with constant surface heat flux. Legends for (a),

305　(b), and (c): dark and light blue represent the results at 09:30 and 12:30, respectively, and the

306　orange and red lines show the results at 15:30 and 18:30, respectively. (d) The kinematic heat flux

307　for all of the runs.

308　　The observation profiles (solid lines in Fig. 4a) show that the depth of the

309　convective boundary layer (CBL) over the grassland increases from 700 m at 09:30 to

310　1.1 km at 12:30 to 1.5 km at 15:30 to 1.9 km at 18:30. The inversion layer above the

311　CBL is completely eroded by the turbulence after 12:30. The virtual potential

312　temperature in the well-mixed CBL over the grassland increases approximately 7 K

313　from 09:30 to 18:30. The CBL over the heterogeneous surfaces with background wind

314　is cooler and shallower than that over the homogeneous surfaces. This may be

315　because the background wind weakens the boundary-layer convection, which inhibits

316　the development of the CBL (Huang et al., 2009). In addition, the model profiles of

317　the virtual potential temperatures over the homogeneously heated and

318　heterogeneously heated surfaces with no background wind have very similar

319　structures and are close to the sounding profiles. This is similar to the modeling

320　results of Liu et al. (2011). The observed virtual potential temperature over the lake

321　surface (solid lines in Fig. 4b) shows that the CBL changes to stable stratification as

322　the radiation increases after sunrise, and the modeled θ_v over the patches is about

323　1.0 K warmer than the observed θ_v. As in Fig. 4a, Fig. 4c also shows that the

324　background wind over the heterogeneous surface inhibits the growth of the CBL.

325　　In this study, according to Sullivan et al. (1998), the height of the boundary layer (z_i)

was determined using the minimum kinematic heat flux of the simulated results. As can be seen, the maximum surface heat flux were relatively large over the homogeneously heated surface, while smaller surface heat flux occurred for the case with two lake patches. Compared to the unbalanced cases (A1L, A1LW, A2L, and A2LW), less heat flux was introduced in the balanced cases (A1LC, A1LWC, A2LC, and A2LWC) and lower CBLs occurred, especially with a wind field (blue bars in Fig. 5). The kinematic heat flux decreased to zero at higher altitude over the heterogeneously heated surface. The region of negative heat flux above that altitude is often called the entrainment layer, which is thicker in the cases with background wind. The heights of the CBL indicate (Fig. 5) that the surface heat flux anomaly may contribute to the deepening of the mixed layer, thus increasing the CBL height. However, the shear generated by the background wind strengthens the turbulent exchange between the entrainment layer and the free atmosphere, resulting in an excessively thick entrainment layer, which, however, inhibits the upward development of CBL.
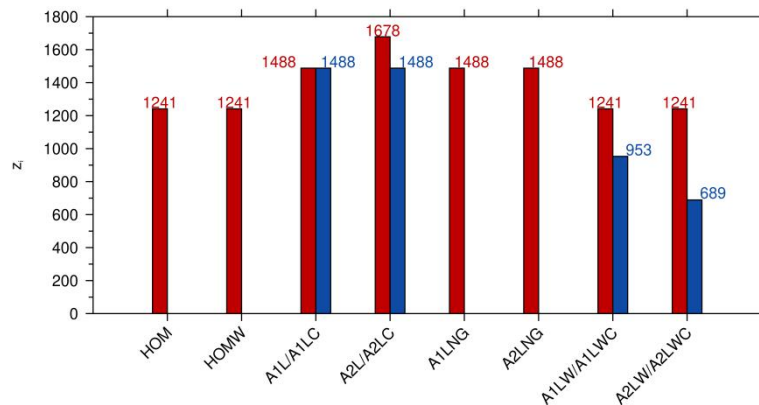

Figure 5. Bar chart of the CBL height for each run marked with a concrete value. The red bars from left to right represent runs HOM, HOMW, A1L, A2L, A1LNG, A2LNG, A1LW, and A2LW. The blue bars from left to right represent runs A1LC, A2LC, A1LWC, and A2LWC.

3.2.2 Effects of the surface heat flux anomalies and background wind on the TKE

Local circulations will be induced by differential heating, and the TKE determines the transport of the momentum, heat, and moisture through the boundary layer (Tyagi and Satyanarayana, 2013). Thus, the thermal circulations induced by the lake patches were simulated to investigate the effects of the heterogeneous heating on the spatial distribution of the TKE.

Fig. 6 shows the vertical distribution of the TKE and the wind vectors over the homogeneous and heterogeneous surfaces with and without background wind at 15:30 LT. Over the homogeneous surface (Fig. 6a), a relatively uniform TKE with a larger magnitude exists within a much shallower CBL (below 0.1 z_i), which overlies the scattered and disordered wind vectors throughout the domain. Over the heterogeneous surfaces, the large TKE values are distributed on both sides of the lake patches below 0.5 z_i, and the divergent winds extend to about 30 km away. In addition, a larger TKE and convergent winds occurred in the upper level of the CBL (Figs. 6b, 6c). Moreover, the air flow between the two lake patches led to a convergent region (updrafts in y= 0 km; Fig. 6c). This is consistent with the results of Avissar and Schmidt (1998), who demonstrated that turbulent eddies are randomly distributed over a homogeneous surface, but the TKE exhibits two maxima near the ground surface and the top of the CBL, which is in agreement with the patch-induced circulations. The similar TKE distribution occurs when the background wind exists over the homogeneous surface (Figs. 6a and 6d). It should be noted that there is larger TKE over the patch/patches (below 0.2 z_i) as the similar pattern of TKE in Papangelis et al. (2021), from which

the TIBL can be recognized (Figs. 6e and 6f). Moreover, the background wind inhibits the development of the patch-induced circulation because the divergent wind derived from the heterogeneous surface can not be viewed at 15:30. Overall, Figure 6 illustrates that the distributions of the TKE and the patch-induced circulations are symmetrical on both sides of the lake patches, while the distribution is random with smaller TKE values over the homogeneous surface. The background wind tends to reduce the TKE outside patch/patches while enhance it over the patch/patches.

Furthermore, the ratios of the horizontally averaged TKE in the model domain of the different runs were calculated to examine the effects of the surface anomalies and the background wind on the TKE. As is shown in Table 2, the TKE for the cases with one or two lake patches are about twice that of the TKE of the case without patches (columns 2–3), but the background wind leads to a reduction in the impacts of surface flux heterogeneity on the TKE (columns 4–5 and 6–7). This is consistent with the results of Avissar and Schmidt (1998), who reported that a weak background wind of 2.5 m/s is strong enough to considerably reduce the impact of the surface heterogeneity on the CBL. For the homogeneous cases, the TKE increases under the background wind conditions due to the increase in the sheared turbulence. For the runs with balanced surface heat flux (A1LC, A2LC, A1LWC, A2LWC), the effects of the heterogeneity on the TKE are less significant due to the relative smaller surface heat flux, especially for the cases with more lake patches, but the effects of the background wind on the TKE tend to be large.
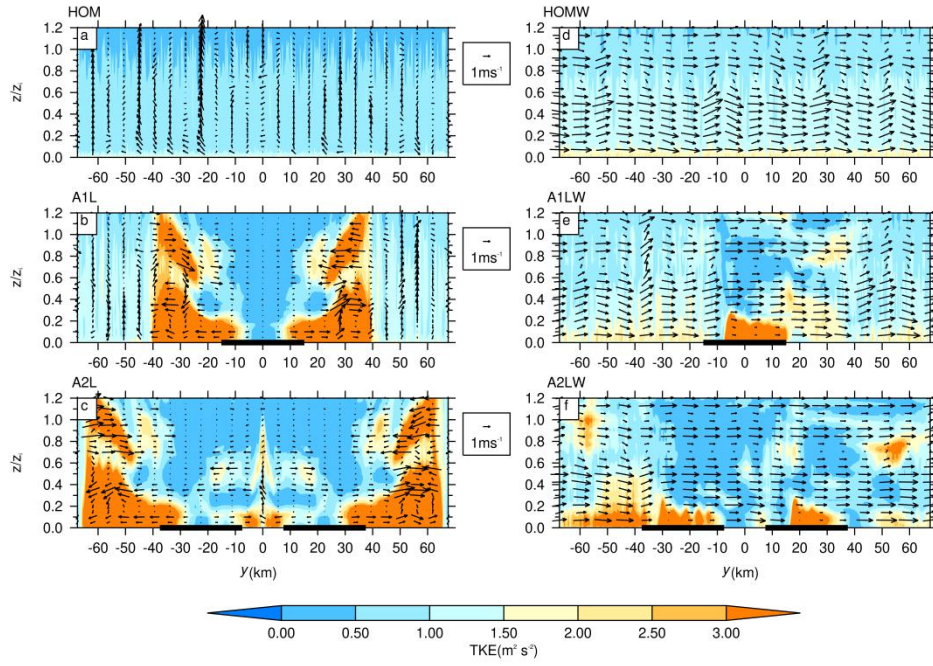
Figure 6. The y-z cross sections of the TKE (contour) with superimposed wind vectors composed of *v* and *w* wind for runs with (d, e, f) and without (a, b, c) background wind over homogeneous (a, d) and heterogeneous (b, e and c, f) surfaces. The thick black lines on the y-axis represent the lake patches.

Table 2

The ratio of the TKEs of the different runs. Max, Min, and Mean stand for the maximum, minimum, and mean ratios of the TKE in the model domain, respectively.

Ratio of TKE	A1L/HOM	A2L/HOM	A1LW/HOMW	A2LW/HOMW	A1LW/A1L	A2LW/A2L	HOMW/HOM
Max	3.31	3.30	1.47	1.42	1.01	0.88	2.09
Min	1.15	1.18	0.80	0.59	0.61	0.40	0.83
Mean	2.00	2.04	1.09	0.95	0.79	0.68	1.41
Ratio of TKE	A1LC/HOM	A2L/HOM	A1LWC/HOMW	A2LWC/HOMW	A1LWC/A1LC	A2LWC/A2LC	HOMW/HOM
Max	2.21	1.44	1.12	0.74	1.84	2.17	2.09
Min	0.43	0.23	0.63	0.31	0.80	0.47	0.83
Mean	1.09	0.75	0.91	0.54	1.22	1.07	1.41

To further investigate the effects of the surface heat flux anomalies on the development of turbulence, it is instructive to examine the vertical profiles of the buoyancy and shear production terms in the TKE budget equation, which is from the

397   contributions of the resolved (RES) and subgrid (SGS) eddies at 15:30 LT (Figs. 7a,

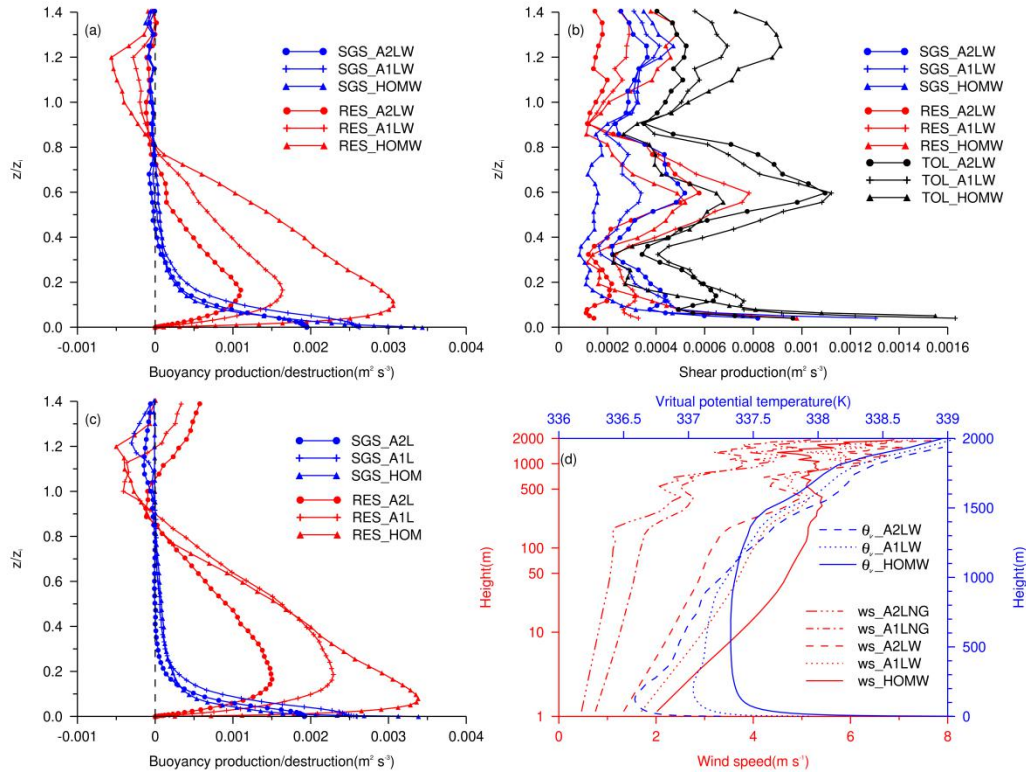398   7b, and 7c).

399   **Figure 7.** Vertical profiles of the buoyancy flux (a) and the shear production term (b) for runs

400   HOMW, A1LW, and A2LW with background wind, and the profiles of the buoyancy flux (c) for

401   runs HOM, A1L, and A2L without background wind. (d) The simulated mean wind versus

402   logarithm of height for runs HOMW, A1LW, A2LW, A1LNG and A2LNG, and the virtual

403   potential temperature profiles (blue line) at the same time (15:30 LT). The resolved and subgrid

404   results are presented as red and blue lines, respectively. The black lines in (b) are the total

405   (resolved and subgrid scale) shear production term.

406   Figures 7a and 7c show that the RES buoyancy production/destruction decreases as

407   the number of patches increases and the SGS buoyancy contributions are negligible,

408   except in the surface layer. The buoyancy production/destruction in the TKE budget

409   equation is $B = \dfrac{g}{\theta_v} \overline{w' \theta_v'}$. The RES buoyancy production/destruction profiles show

410   that the lower maximum occurs for the wind simulations over the heterogeneous

411 surfaces. It is because the larger positive buoyancy production/destruction decreases,

412 especially in the downstream of the patch (Fig. S4 in the supplement), which is due to

413 the significantly weakened updrafts of the patch-induced circulations by the

414 background wind. Comparing with no wind simulations (Figs. S4b, S4c), the

415 buoyancy production/destruction over the patch/patches decreases for wind

416 simulations. It is probably caused by the relatively warm air in a thermal internal

417 boundary layer (TIBL) formed over the patch/patches (Figs. S5b, S5c) due to the

418 abrupt change in surface heat flux (Mahrt, 2000) with air flowing from the warm

419 patch to the cold patch. Similar with the results of Zhou et al. (2018) and Liu et al.

420 (2020), the cold center of the TIBL (Figs. S5e, S5f) moves to the downwind of the

421 lake patches. Below 0.9 z_i, the larger RES shear production occurs in the case with

422 lake patches (Fig. 7b) and the contribution of the SGS shear production is

423 considerable (Fig. 7b), which is significant in the CBL for the cases with surface flux

424 anomalies. Thus, the total shear productions (black lines in Fig. 7b) of the cases with

425 heterogeneous surfaces are larger. In addition, wind shear is the source of the SGS

426 shear production peak at $z/z_i = 0.6$ due to the larger momentum flux above 0.6 z_i (see

427 Fig. S3) increasing the wind speed and wind shear below. Fig. 7d showed the wind

428 profiles (red lines) for runs with background wind (HOMW, A1LW, A2LW) and

429 without geostrophic wind (A1LNG, A2LNG), and the virtual potential temperature

430 profiles (blue lines). It shows that patch-induced circulations reduce the modeled

431 mean wind speed below the height of about 800 m, for the largest wind speed exists in

432 the homogeneous case (red solid line). The wind profile is log-linear below the height

433   of 20 m and shows a clear mixed layer above it for the homogeneous run, which

434   correspond to a mixed layer shown by the virtual potential temperature profile (blue

435   solid line). For the one/two-lake simulations, the wind profiles (red dotted and dashed

436   lines) exhibit a feature of a stable boundary layer (blue dotted and dashed lines) with a

437   maximum local wind at about 400 m. It should be noted that the stable stratification of

438   wind profiles between 200 m and 1000 m are probably caused by the process of the

439   TIBL. It is confirmed by the similar wind profile features from the runs without

440   geostrophic wind over the heterogeneous surface.

441   **3.2.3 Effects of the background wind on the circulations**

442   In order to investigate the effects of the background wind on the patch-induced

443   circulations, the vertical distributions of the vertical velocity and wind fields for the

444   runs with and without background wind were compared. In Fig. 8, the patch-induced

445   circulations are not easy to distinguish in the cases with background wind (about 13.9

446    $m \cdot s^{-1}$ above a height of 1.2 km) due to the cancellation of the local pressure gradient

447   by the synoptic pressure gradient, which is consistent with the results of Crosman and

448   Horel (2010). This also indicates that the boundary-layer convection tends to weaken

449   as the number of lake patches increases (the maximum updrafts are 4.8 $m \cdot s^{-1}$, 4.2 $m \cdot s^{-1}$,

450   3.5 $m \cdot s^{-1}$, and 3.3 $m \cdot s^{-1}$ for runs A1L, A2L, A1LW, and A2LW, respectively), which is

451   confirmed by the weaker buoyancy production/destruction for the heterogeneous

452   simulations in the Figs. 7a and 7c. Moreover, the wind fields for the cases without

453   geostrophic winds exhibit divergent flows over the lake patches. As in the study of

454   Kang and Lenschow (2014), our study also confirms that the symmetrical

455 patch-induced circulations and the intensity of the convection become

456 indistinguishable and weak under the background wind conditions. However, the

457 divergent flows in the lower level are still visible when the geostrophic wind is

458 removed (A1LNG and A2LNG in Figs. 8e and 8f). Comparing with the spatial

459 distribution of the vertical velocity over the homogeneous surface (Figs. 8g and 8h),

460 the lake patch/patches alters both the boundary-layer convection intensity and the

461 local circulation.
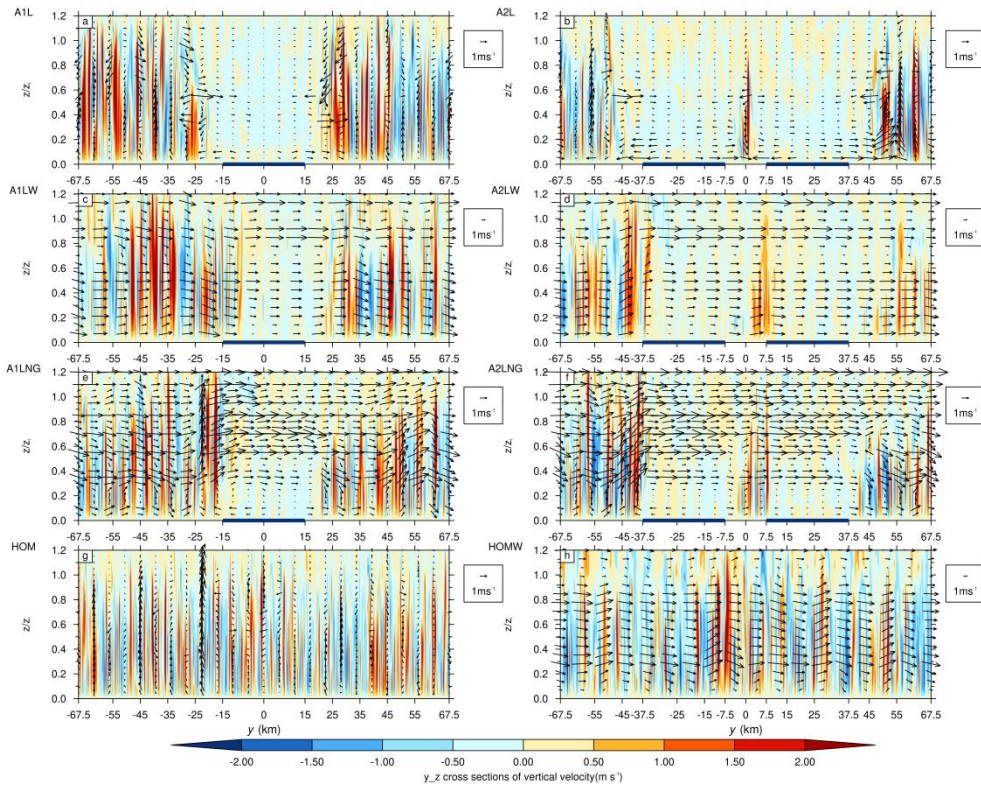
462 **Figure 8.** Instantaneous y-z cross sections of the vertical velocity (m·s^{-1}) and wind vectors above

463 the heterogeneous surfaces for runs without (a and b) and with (c and d) background wind, and

464 with the geostrophic wind removed (e and f), as well as the results over homogeneous surfaces for

465 runs with (h) and without (g) background wind. The blue lines represent the lake patches.

466 **3.3 Effects of patch-induced circulation on the turbulent intensity**

467 **and heat flux**

468   We used the phase-averaged method to decompose the contributions of the

469   turbulent intensity and the heat flux from the patch-induced circulations and the

470   background turbulence and to quantitatively analyze the heterogeneity-induced

471   contribution to the turbulent intensity. For the variance of the velocity, the horizontal

472   (Fig. 9a) and vertical (Fig. 9b) variances induced by the heterogeneity increase as the

473   number of lake patches increases, and the horizontal variance is larger than the

474   vertical variance. However, the background wind tend to decrease both the

475   patch-induced (Figs. 9a, 9b) and total (Figs 9e, 9f) turbulent intensity.
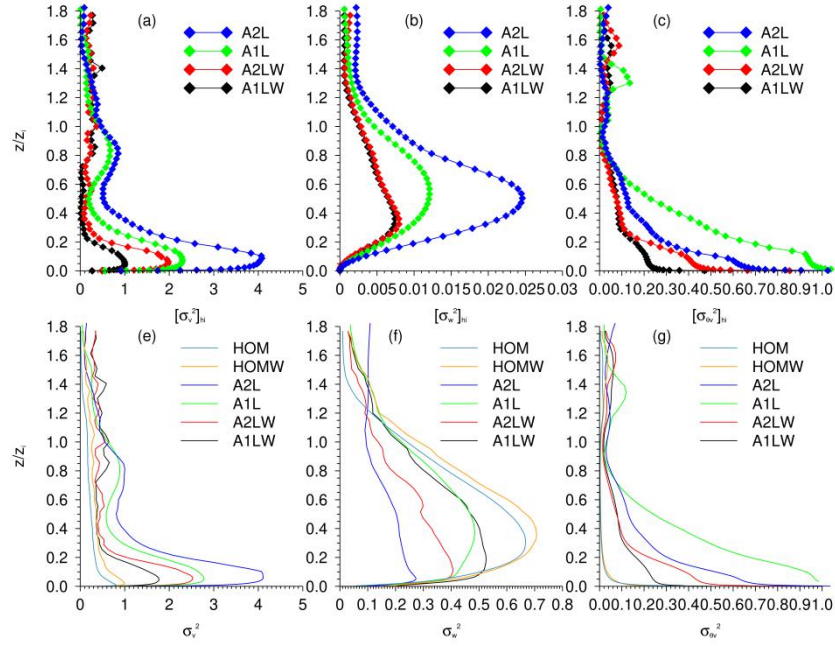
476   **Figure 9.** Heterogeneity-induced (a, b, c) and total (e, f, g) dimensionless turbulence statistics for

477   runs HOM, HOMW, A1L, A1LW, A2L, and A2LW. Shown are the profiles of the (a, e) v variance,

478   (b, f) w variance, and (c, g) θ variance.
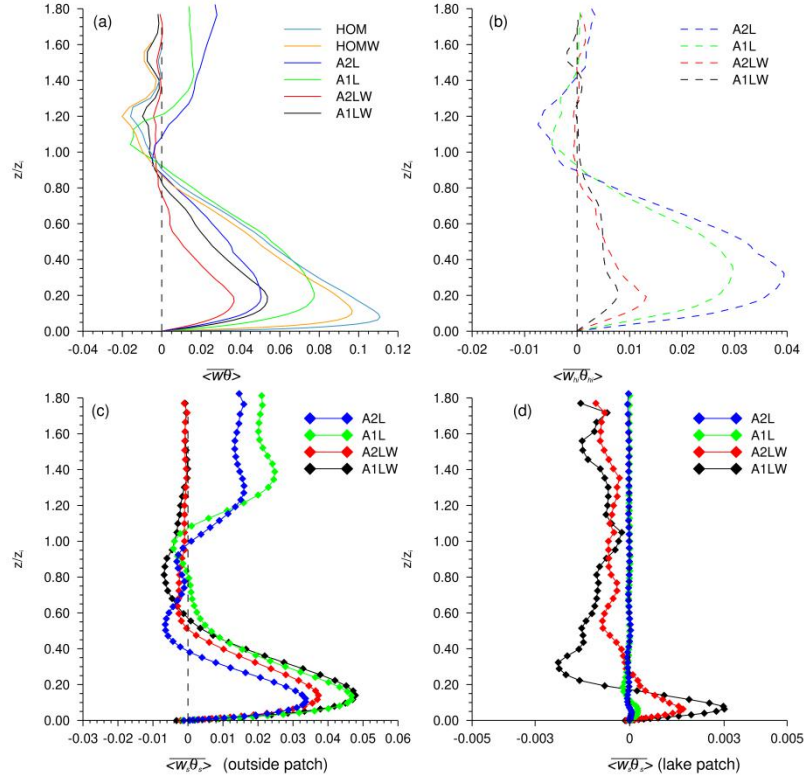
Figure 10. (a) Area-averaged total turbulent heat flux (solid lines) and (b) heterogeneity-induced turbulent heat flux (dash lines). The background turbulence (lines with diamond symbols) of heat flux over the grassland (c) and lake patches (d).

This also shows that a larger difference in the variances of the horizontal velocity occurs in the surface layer and gradually decreases with height (Figs. 9a and 9e), which means that the effects of the surface properties on the horizontal turbulence diminish with height in the CBL. In this respect, our results are similar to those found by Wang et al. (2011), Shao et al. (2013), and Frederik and Matthias (2018). The total horizontal turbulent intensity is mainly from the contribution of the patch-induced circulations and is larger than that of the homogeneous cases (Fig. 9e), which tends to become stronger as the number of patches increases but becomes weaker as the total vertical turbulent intensity increases (Fig. 9f, same as in the cases with balanced surface fluxes). It should be noted that the contribution of the patch-induced

27

492　circulations to the vertical velocity variance is no more than 10% (Fig. 9b and 9f),

493　which implies that the background turbulence contributes more to the fluctuations in

494　the vertical velocity than to those in the horizontal velocity. Figures 9c and 9g show

495　that the patch-induced motions make the largest contribution to the variances of the

496　potential temperature. However, the background wind decreases the variances of the

497　potential temperature and decrease the impact of the surface heterogeneity on the

498　variances of the potential temperature.

499　　Using the same method, we analyzed the contributions of the patch-induced and

500　background turbulence to the heat flux. Figure 10a shows that as the number of lake

501　patches increases, the area-averaged total heat flux decreases in both the mixed and

502　entrainment layers, and the balanced surface heat flux cases exhibit similar variations

503　(see Fig. S6 in supplement). The patch-induced transport of the heat flux increases as

504　the number of lake patches increases (Fig. 10b). The patch-induced motions

505　contribute up to 80% of the heat flux in run A2L, which has unbalanced surface fluxes

506　(Fig. 10b), and 61% in run A2LC which has balanced surface fluxes (see Fig. S6 in

507　supplement). It should also be noted that the background wind tends to decrease the

508　heat flux transport over the heterogeneous surfaces. As is shown in Figs. 10c and 10e,

509　the contribution of the background turbulence to the local heat flux is larger over the

510　region outside of the lake patches than over the patches. Notice that the minimum heat

511　flux (Fig. 10d, at about 0.3 z_i) is in the magnitude so strong as it is close to the surface

512　(0.1 z_i). It probably contributes the local maximum wind speed. We hope that the

513　results of our analysis of the contributions of the heterogeneity-induced circulation

514 and background turbulence to the turbulence intensity and the heat flux over a

515 heterogeneous surface will provide a basis for further studies of the local energy and

516 mass transport in the SRYR over the TP.

3.4 Turbulence in the surface layer
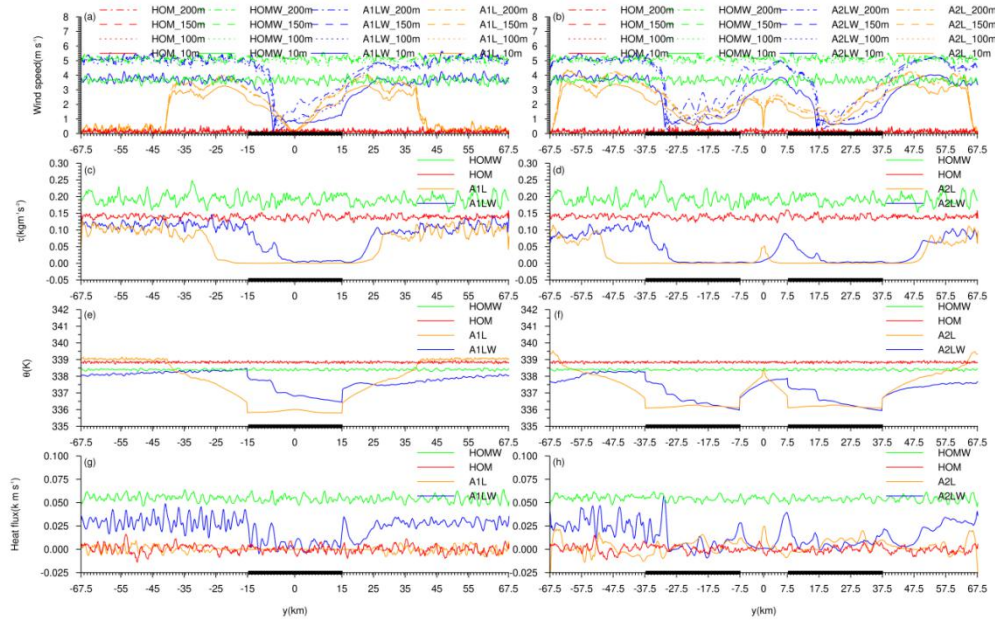
517

518 **Figure 11.** Variations in the wind speed (a and b) and Reynolds stress (c and d), potential

519 temperature (e and f) and heat flux (g and h) in the horizontal direction below 200 m for the cases

520 with (blue and green lines) and without (yellow and red lines) background wind over

521 homogeneous (red and green lines) and heterogeneous (blue and yellow lines) surfaces. Thick

522 black lines represent the lake patches.

523 The frictional velocity (u_*) is a critical parameter in the turbulence exchange near

524 the surface, and it plays an important role in the transport of momentum in the

525 boundary layer. Patil et al. (2016) reported that the frictional velocity increases with

526 wind speed under lower wind speed conditions in the surface layer. Thus, we focused

527 on the variations in the wind speed (Figs. 11a and 11b) and Reynolds stress (Figs. 11c

528 and 11d) in the horizontal direction below 200 m in order to investigate the effects of

529   the patch-induced motions on the momentum flux in the surface layer for various

530   background wind. It was found that the inland extension of the patch-induced

531   divergent flows reached about 25 km with no background wind (yellow curves in Figs.

532   11a and 11b). The speed of the divergent winds increases from the lake patches to the

533   outside and increases with height below 200 m with and without background wind.

534   The wind speeds decrease rapidly ($4.0 \ m \cdot s^{-1}$) within 10 km along with the wind

535   blowing from west of the lake patches to east of the lake patch, and then, the wind

536   speeds increase steadily (blue curves in Figs. 11a and 11b). The changes in the surface

537   winds and surface properties have significant effects on the turbulent momentum flux.

538   Figures 11c and 11d show that the transport of the momentum flux is smaller over the

539   heterogeneous surface. The consistent variations in the wind speeds and the turbulent

540   stresses illustrate that the lake patches alter the spatial distribution of the turbulent

541   stress, which would further affect the surface wind speeds, especially over the

542   land-lake boundary regions. Moreover, the potential temperature (Figs. 11e, 11f) and

543   the sensible heat flux (Figs. 11g, 11h) increase abruptly from the lake patch to the

544   grass patch (e.g. from y=15 km to y=25 km in Fig. 11e), which indicates the
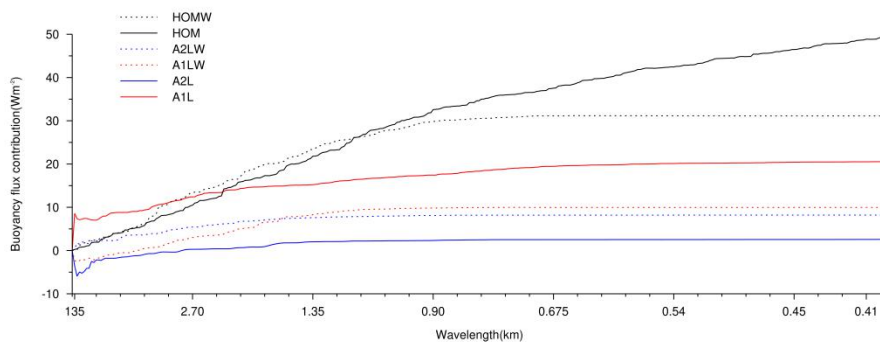
545   formation of the TIBL.

In order to quantify the contributions of the buoyancy fluxes, due to the different scales of the eddies, we calculated the ogives, which are the running integrals of the cospectral densities (Friehe et al., 1991), and used these values to show the cumulative contribution to the fluxes of all of the wavelengths (Brooks and Rogers, 2000). The ogives curves (Fig. 12) show that the small eddies make a significant contribution to the buoyancy fluxes over the homogeneous surfaces with no background wind (solid black line). The background wind increases the buoyancy flux for wavelengths larger than about 1.1 km and decreases it for smaller wavelengths based on a comparison of cases HOM (solid black line) and HOMW (black dotted line). The above results confirm that the heat transport is enhanced by the large eddies but is weakened by the small eddies, especially under the control of the background wind. The buoyancy flux for a wavelength larger than about 2.2 km makes a greater contribution in the case with one lake patch without background wind (solid red line). The buoyancy fluxes for wavelengths of greater than 2.7 km are transported downward for the case with two lake patches. For the case with one lake patch, the background wind tends to decrease the transport of the buoyancy flux for larger wavelengths near the surface (red dotted line) due to the stronger horizontal wind (Fig. 7d), and they help to transport the buoyancy fluxes downward for wavelengths larger than 3.3 km. However, for the case with two lake patches, the background wind causes the large eddies to transport the buoyancy fluxes upward. Thus, increasing the number of lake patches leads to more patch-induced motions, but

569   this does not tend to enhance the ability of the wind to transport heat. It is concluded

570   that slightly more of the buoyancy flux of the case with one lake patch is transported

571   by the small eddies with wavelengths of less than 1.5 km compared with the case with

572   two lake patches and background wind conditions (red and blue dotted lines).

3.5 The characteristics of the boundary-layer turbulence in the entrainment layer

575   The LES study conducted by Matthias et al. (2014) found that there is increased

576   entrainment from the more strongly heated surface patch cases compared to the

577   homogeneous cases, and the impact of the heterogeneity on entrainment vanishes due

578   to horizontal mixing if the mean flow is aligned perpendicular to the border between

579   the differentially heated patches. To investigate the effects of the thermal properties of

580   the heterogeneous surface and the background wind on the turbulence in the

581   entrainment layer, the characteristics of the heat flux in the entrainment layer were

582   analyzed. Our simulated results show that the downward transport of the heat flux

583   decreases as the number of lake patches increases in the entrainment layer for both the

584   wind and no wind cases (Figs. 4d and 10a), which is also true in the balanced heat

585   flux runs.

586   By comparing the maximum and minimum vertical velocities at the top of the

587   boundary layer (Table 3), we found that the convective intensity of the entrainment

588   layer in the case with two lake patches and no wind fields is stronger, but it is

589   weakened by the background wind. Whereas, it decreases as the number of lake

590   patches increases in the balanced heat flux cases (A1LC and A2LC), corresponding to

591 a smaller TKE (Table 2) and total turbulent intensity (Fig. 9f). Huang et al. (2009)

592 pointed out that an appropriate surface heat flux and background wind maintain the

593 convective roll, and our simulations demonstrate this roll-like convection (see Fig. S7

594 in supplement), which is mainly induced by the persistence of the background

595 turbulence with stronger geostrophic winds of 7–11 m·s^{-1} (black lines in Fig. 2g).

596 However, Maronga and Raasch (2013) found that a higher wind speed of 6 m·s^{-1}

597 generates convective rolls derived from the secondary circulation over a complex
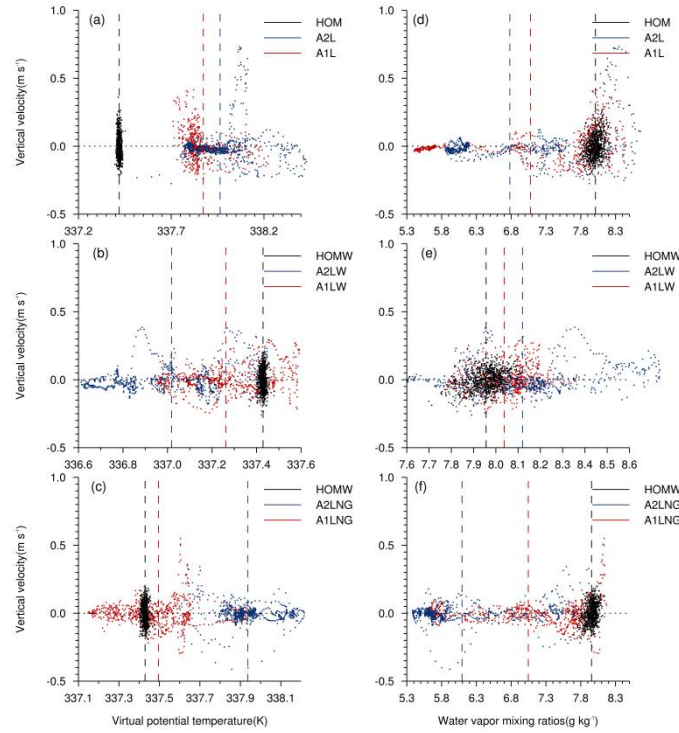
598 heterogeneous surface.

Figure 13. The joint vertical velocities, virtual potential temperatures (a, b, c) and water vapor mixing ratios (d, e, f) at the top of the CBL for the homogeneous runs (black dot) and heterogeneous runs (red for one-lake and blue for two-lakes). The black dotted lines represent the mean vertical velocity, the black, red and blue dashed lines show the mean virtual potential temperatures and water vapor mixing ratios for the homogeneous, one-lake and two-lakes runs, respectively.

605   In addition, the boundary layer variables (including the vertical velocities, virtual

606   potential temperatures, and water vapor mixing ratios) in the entrainment layer are

607   also subject to the effects of the surface heterogeneity. Figure 13 shows the joint

608   distribution of the vertical velocities and the virtual potential temperatures, as well as

609   the vertical velocities and water vapor mixing ratios. Comparing to the

610   homogeneously heated cases, the increased downdrafts mainly occur over the lake

611   patches, and they carry more warm, dry air down from the free atmosphere (Figs. 13a,

612   13b, 13g, and 13h), which is due to the convergent airflow caused by the

613   patch-induced circulations at the top of the CBL. This effect is much more evident in

614   the case with two lake patches, but it is weakened by the gradually strengthening

615   background wind (except Figs. 13a, 13b, 13g, and 13h). We obtained the same results

616   for the balanced cases. In particular, colder and moister air exists in the entrainment

617   layer in the cases with background wind (A1LWC and A2LWC).

618   **Table 3**

619   The maximum and minimum vertical velocities at the top of the boundary layer in cases A1LW,

620   A2LW, A1LWC, A2LWC, A1LNG, A2LNG, A1L, A2L, A1LC, A2LC and HOM, HOMW.

Case	A1LW	A2LW	A1L	A2L	HOM	HOMW
W(max)	4.01	3.54	5.42	5.55	4.37	4.48
W(min)	−2.29	−1.98	−2.40	−3.12	−2.15	−2.50
Case	A1LWC	A2LWC	A1LC	A2LC	A1LNG	A2LNG
W(max)	2.97	2.06	4.26	2.46	3.90	4.46
W(min)	−2.03	−1.25	−1.91	−1.27	−2.23	−1.97

621   # 4   Summary and discussion

622   The downdrafts and divergent zonal wind in the two lakes area obtained from the

623   ERA-Interim reanalysis data indicate the existence of a lake breeze in the SRYR. Ten

runs of the 1D strip-like distribution of the surface heat flux and two homogeneous

runs based on the observations made during the summer of 2012 in the Ngoring Lake

Basin were conducted in order to investigate the effects of the patch-induced

circulations on the boundary-layer turbulence and its energy transport at the lake-air

and grass-air interfaces, and the influence of the background wind also be considered.

The thermodynamic heterogeneity of the surface is conducive to deepening the

mixed layer, thus increasing the CBL height and enhancing the TKE when there are

no background wind. The background wind brings shear, resulting in an excessively

thick entrainment layer, which inhibits the growth of CBL and reduce the effects of

the heterogeneous surface on the TKE. The distribution of the TKE over the

heterogeneous surface is consistent with the patch-induced circulations described by

Avissar and Schmidt (1998). In addition, the enhanced effects by surface heat

anomaly on the TKE are far lower in the cases with an balanced surface heat flux. By

analyzing the buoyancy and shear production terms in the TKE budget equation and

separating the contribution of the resolvable-scale (RES) and subgrid-scale (SGS)

eddies, we found that the contributions of the wind shear to the TKE from the SGS

eddies are considerable in the CBL (below 0.9 z_i) over a heterogeneous surface. The

patch-induced circulations reduce the modeled mean wind speed. The clear mixed

layer is shown by the wind and virtual potential temperature profiles for the

homogeneous run, while the stable stratification of wind profiles for the

heterogeneous simulations are probably caused by the process of the TIBL. We

obtained the same conclusion as Kang and Lenschow (2014), that is, the

646 patch-induced circulations become indistinguishable under background wind

647 conditions, and the background wind also weakens the convective intensity.

648 Then, we conducted a phase-averaged analysis to separate the contributions of the

649 turbulent intensity and the transport of the total heat flux from those of the

650 patch-induced circulations and the background turbulence field. The patch-induced

651 turbulent intensity increases with increasing lake patches. It mainly contributes to the

652 horizontal turbulent intensity and the potential temperature variance, while it

653 contributes no more than 10% to the vertical turbulent intensity, of which the

654 background turbulence contributes the most. The background wind weakens the

655 patch-induced and horizontal turbulent intensities but strengthen the vertical turbulent

656 intensity. The contribution of the patch-induced heat flux was up to 80% in the

657 unbalanced cases and 60% in the balanced cases. The background turbulence made a

658 larger contribution to the heat flux over the outside of patches, which have a stronger

659 surface heat flux than that over the lake patches. The background wind also inhibits

660 the transport of the heat flux.

661 To understand the effects of the patch-induced motions on the momentum flux in

662 the surface layer under various background wind conditions, we focused on the

663 variations in the wind speed and the Reynolds stress in the horizontal direction below

664 200 m. Without background wind, the inland extent of the patch-induced flows was

665 about 25 km. When the background wind flowed into the lake patches, they decreased

666 by 4.0 $m \cdot s^{-1}$ within about 10 km and increased steadily when flowing out of the

667 patches. The synchronized variations in the wind speed and momentum flux in the

668　horizontal direction illustrate that the lake patches alter the spatial distribution of the

669　turbulent stress, which further affects the surface wind speeds, especially over the

670　land-lake boundary regions. We also analyzed the cumulative contribution of eddies

671　with different scales to the buoyancy flux near the surface. It was found that without

672　background wind, the buoyancy flux is transmitted upward by the eddies with larger

673　wavelengths for the case with one lake patch; while there is a negative buoyancy flux

674　in the case with two lake patches. Thus, increasing the number of lake patches leads

675　to more patch-induced motions, which do not tend to enhance the heat transport

676　ability. The background wind promotes the opposite results.

677　　In the entrainment layer, in contrast to Matthias et al. (2014) who found that the

678　entrainment increased for the stronger heated surface patch cases compared to the

679　homogeneous case, we found that the entrainment flux decrease as the number of lake

680　patches increases. For the unbalanced cases, the convective intensity increases as the

681　number of lake patches increases, but the background wind weakens it. For the

682　balanced cases, the convective intensity weakens as the number of lake patches

683　increases, corresponding to a smaller TKE and total turbulent intensity. In this study,

684　whether the convective rolls persist mainly depended on the background turbulence

685　field with a higher geostrophic wind of 7–11 $m \cdot s^{-1}$, while Maronga and Raasch (2013)

686　reported a higher wind speed of 6 $m \cdot s^{-1}$. As the number of lake patches increases, the

687　increased downdrafts are mainly located over the lake patches, and they carry more

688　warm, dry air down from the free atmosphere in both the balanced and unbalanced

689　cases. The background wind weakens this effect even when there is cooler, moister air

690   in the entrainment layer in the balanced cases.

691   Our study provides ideal simulations of the boundary-layer turbulence over the

692   heterogeneous surface in the SRYR. It mainly focused on the influences of the

693   heterogeneous distribution of the surface heat flux and the background wind. In the

694   future, we plan to conduct further research that will take into consideration the

695   topography and additional physical processes to provide a reference for the study of

696   the energy and water exchange processes over the complex surface of the SRYR.

References

717   Avissar, R., and Pielke, R. A.: A Parameterization of Heterogeneous Land Surfaces for

718   Atmospheric Numerical Models and Its Impact on Regional Meteorology,

719   Monthly   Weather   Review,   117(10),   2113-2136.

720   doi:10.1175/1520-0493(1989)117<2113:APOHLS>2.0.CO;2, 1989.

721   Avissar, R., and Schmidt, T.: An Evaluation of the Scale at which Ground-Surface

722   Heat Flux Patchiness Affects the Convective Boundary Layer Using Large-Eddy

723   Simulations, Journal of the Atmospheric Sciences, 55(16), 2666–2689.

724   doi:10.1175/1520-0469(1998)055<2666:AEOTSA>2.0.CO;2, 1998.

725   Ao, Y. H., Lyu, S. H., Li, Z. G., Wen, L. J., and Zhao, L.: Numerical simulation of the

726   climate effect of high-altitude lakes on the Tibetan Plateau. Sciences in Cold and

727   Arid Regions, 10(5): 0379－0391. doi: 10.3724/SP.J.1226.2018.00379, 2018.

728 Biermann, T., Babel, W., Ma, W. Q., Chen, X. L., Thiem, E., Ma, Y. M., and Foken, T.:

729   Turbulent flux observations and modelling over a shallow lake and a wet

730   grassland in the Nam Co basin, Tibetan Plateau. *Theor. Appli. Clima.*, **116**,

731   301-316, doi: 10.1007/s00704-013-0953-6, 2014.

732 Brierley, G. J., Li, X., Cullum, C. and Gao, C. (Eds.): Landscape and Ecosystem

733   Diversity, Dynamics and Management in the Yellow River Source Zone,

734   Springer International Publishing, 2016.

735 Brooks, I. M., and Rogers, D. P.: Aircraft observations of the mean and turbulent

736   structure of a shallow boundary layer over the Persian Gulf [J]. Bound.-Layer

737   Meteor., 95(2): 189－210. doi:10.1023/A:1002623712237, 2000.

738 Brown, A. R., Derbyshire, S. H. and Mason, P. J.: Large-eddy simulation of stable

739   atmospheric boundary layers with a revised stochastic subgrid model. *Quart. J.*

740   *Roy.*   *Meteor.*   *Soc.*,   120(520),   1485-1512,

741   https://doi.org/10.1002/qj.49712052004, 1994.

742 Chen, X., Añel, J. A., Su, Z. B., Torre, L. D. L., Kelder, H., Peet, J. V., and Ma, Y. M.,

743   The Deep Atmospheric Boundary Layer and Its Significance to the Stratosphere

744   and Troposphere Exchange over the Tibetan Plateau. *PLoS ONE,* **8**, e56909,

745   https://doi.org/10.1371/journal.pone.0056909, 2013.

746 Chen, X., Škerlak, B., Rotach, M. W., Añel, J. A., Su, Z. B., Ma, Y. M., and Li, M. S.:

747   Reasons for the extremely high-ranging planetary boundary layer over the

748   western Tibetan Plateau in winter. *J. Atmos. Sci.*, **73**, 2021-2038, doi:

749   10.1175/JAS-D-15-0148.1, 2016.

750   Crosman, E. T., and Horel, J. D.: Sea and Lake Breezes: A Review of Numerical

751   Studies. *Bound.-Layer Meteor.*, 137(1), 1 – 29. doi:10.1007/s10546-010-9517-9,

752   2010.

753   Crosman, E. T., and Horel, J. D.: Idealized Large-Eddy Simulations of Sea and Lake

754   Breezes: Sensitivity to Lake Diameter, Heat Flux and Stability.   *Bound.-Layer*

755   *Meteor.*, **144**, 309-328, https://doi.org/10.1007/s10546-012-9721-x, 2012.

756   Friehe, C. A., Shaw, W. J., Rogers, D. P., Davidson, K. L., Large, W. G., Stage, S. A.,

757   Crescenti, G. H., Khalsa, S. J. S., Greenhut, G. K., and Li, F.: Air-sea fluxes and

758   surface layer turbulence around a sea surface temperature front [J]. J. Geophys.

759   Res., 96(C5): 8593 – 8609. doi:10.1029/90JC02062, 1991.

760   Foken, T., Matthias, M., Liebethal, C., Wimmer, F., Beyrich, F., Leps, J. P., Raasch, S.,

761   DeBruin, H. A. R., Meijninger, W. M. L., Bange, J.: Energy balance closure for

762   the LITFASS-2003 experiment. Theor Appl Climatol., 101(1-2), 149-160.

763   doi:10.1007/s00704-009-0216-8, 2010.

764   Gray, M. E. B., Petch, J., Derbyshire, S. H., et al. 2001. Version 2.3 of the Met.Office

765   large eddy model: part Ⅱ. Scientific documentation [R]. Met Office (APR)

766   Turbulence and Diffusion Note No.276.

767   Hadfield, M. G., Cotton, W. R., and Pielke, R. A.: Large-eddy simulations of

768   thermally forced circulations in the convective boundary layer. Part I: A

769   small-scale circulation with zero wind. Boundary-Layer Meteorology, 57(1-2),

770   79-114. doi:10.1007/bf00119714, 1991.

771 Hadfield, M. G., Cotton, W. R., and Pielke, R. A.: Large-eddy simulations of

772   thermally forced circulations in the convective boundary layer. Part II: The

773   effect of changes in wavelength and wind speed. Boundary-Layer Meteorology,

774   58(4), 307-327. doi:10.1007/bf00120235, 1992.

775 Honnert, R., Masson, V., & Couvreux, F.: A diagnostic for evaluating the

776   representation of turbulence in atmospheric models at the kilometric scale. J.

777   Atmos. Sci., 68 , 3112-3131. doi: 10.1175/JAS-D-11-061.1, 2011.

778 Honnert, R., Efstathiou, G. A., Beare, R. J., et al. The Atmospheric Boundary Layer

779   and the "Gray Zone" of Turbulence: A Critical Review. Journal of Geophysical

780   Research: Atmospheres, 125. doi: 10.1029/2019JD030317, 2020.

781 Huang, Q., Marsham, J. H., Parker, D. J., Tian, W. S., Tammy, W.: A Comparison of

782   Roll and Nonroll Convection and the Subsequent Deepening Moist Convection:

783   An LEM Case Study Based on SCMS Data. Monthly Weather Review, 137(1),

784   350-365. doi:10.1175/2008MWR2450.1, 2009.

785 Jia, D., Wen, J., Ma, Y., Wang, X. and Lai, X.: The warm season characteristics of the

786   turbulence structure and transfer of turbulent kinetic energy over alpine

787   wetlands at the source of the yellow river. Meteorology & Atmospheric Physics,

788   130(1), 1-14. doi: 10.1007/s00703-017-0534-9, 2017.

789 Kang, S. L., and Lenschow, D. H.: Temporal evolution of low-level winds induced by

790   two-dimensional mesoscale surface heat-flux heterogeneity. Boundary-Layer

791   Meteorology, 151: 501－529. doi: 10.1007/s10546-014-9912-8, 2014.

792 Li, W. L., Lü, S. H., Fu, S. M., Meng, X. H., and Nnamchi, H. C.: Numerical

simulation of fluxes generated by inhomogeneities of the underlying surface over the Jinta Oasis in Northwestern China. *Adv. Atmos. Sci*, **28**, 887-906, doi: 10.1007/s00376-010-0041-0, 2011.

Li, Z. G., Lyu, S. H., Ao, Y. H., Wen, L. J., Zhao, L., Wang, S. Y.: Long-term energy flux and radiation balance observations over Lake Ngoring, Tibetan Plateau. *Atmos. Res.*, **155**, 13-25, https://doi.org/10.1016/j.atmosres.2014.11.019, 2015.

Li, Z. G., Lyu, S. H., Wen, L. J., Zhao, L., Ao, Y. H., Wang, S. Y.: Effect of a cold, dry air incursion on atmospheric boundary layer processes over a high-altitude lake in the Tibetan Plateau. *Atmos. Res.*, **185**, 32-43, doi: 10.1016/j.atmosres.2016.10.024, 2017.

Liu, G., Sun, J. N., and Yin. L.: Turbulence characteristics of the shear-free convective boundary layer driven by heterogeneous surface heating. Boundary-Layer Meteorology, 140(1), 57-71. doi: 10.1007/s10546-011-9591-7, 2011.

Liu, R., Liu, S.M., Yang, X.F., Lu, H., Pan, X.D., Xu, Z.W., Ma, Y.F., Xu, T.R.: Wind dynamics over a highly heterogeneous oasis area: an experimental and numerical study. J. Geophys. Res. 123, 8418 – 8440. doi: 10.1029/2018JD028397, 2018.

Liu, R., Sogachev, A., Yang, X., Liu, S., Xu, T., Zhang, J.: Investigating microclimate effects in an oasis-desert interaction zone. Agricultural and Forest Meteorology, 290, 107992. doi: 10.1016/j.agrformet.2020.107992, 2020.

Mahrt, L.: Surface Heterogeneity and Vertical Structure of the Boundary Layer. , 96(1-2), 33–62. doi:10.1023/a:1002482332477, 2000.

815   Maronga, B., and Raasch, S.: Large-eddy simulations of surface heterogeneity effects

816   on the convective boundary layer during the litfass-2003 experiment.

817   Boundary-Layer Meteorology, 146(1), 17-44. doi: 10.1007/s10546-012-9748-z,

818   2013.

819   Marsham, J. H., Parker, D. J., Grams, C. M., Johnson, B. T., Grey, W. M. F., and Ross,

820   A. N.: Observations of mesoscale and boundary-layer scale circulations

821   affecting dust transport and uplift over the Sahara. *Atmos. Chem. Phys*, **8**,

822   6979-6993, https://doi.org/10.5194/acp-8-6979-2008, 2008.

823   Matthias, S., Maronga, B., Florian, H., and Siegfried, R.: On the Effect of Surface

824   Heat-Flux Heterogeneities on the Mixed-Layer-Top Entrainment.

825   Boundary-Layer Meteorology, 151(3), 531-556.

826   doi:10.1007/s10546-014-9913-7, 2014.

827   Moeng, C.-H.: A Large-Eddy-Simulation Model for the Study of Planetary

828   Boundary-Layer Turbulence. *J. Atmos. Sci.*, **41**, 2052-2062,

829   https://doi.org/10.1175/1520-0469(1984)041<2052:ALESMF>2.0.CO;2, 1984.

830   Mudassar, I., Wen, J., Wang, S. P., Tian, H., and Adnan, M.: Variations of precipitation

831   characteristics during the period 1960-2014 in the source region of the Yellow

832   River, China. Journal of Arid Land, 10(3): 388-401.

833   https://doi.org/10.1007/s40333-018-0008-z, 2018.

834   Patil, M. N., Waghmare, R. T., Dharmaraj, T., Chinthalu, G. R., Devendraa, S., and

835   Meena, G. S.: The influence of wind speed on surface layer stability and

836   turbulent fluxes over southern Indian peninsula station. Journal of Earth System

837   Science, 125(7), 1399–1411. doi:10.1007/s12040-016-0735-5, 2016.

838   Patton, E. G., Sullivan, P. P., and Moeng, C. H.: The influence of idealized

839   heterogeneity on wet and dry planetary boundary layers coupled to the land

840   surface. Journal of the Atmospheric Sciences, 62(7), 2078-2097. doi:

841   10.1175/JAS3465.1, 2005.

842   Shao, Y. P., Liu, S. F., Schween, J. H., and Crewell, S.: Large-Eddy

843   Atmosphere-Land-Surface Modelling over Heterogeneous Surfaces: Model

844   Development and Comparison with Measurements. Boundary-Layer

845   Meteorology, 148(2), 333-356. doi: 10.1007/s10546-013-9823-0, 2013.

846   Shen, S. H., and Leclerc, M. Y.: How large must surface inhomogeneities be before

847   they influence the convective boundary layer structure? A case study. Q. .I. R.

848   Meteorol. soc., 121(526), 1209-1228. doi:10.1002/qj.49712152603, 1995.

849   Shen, L. D., Sun, J. N., Yuan, R. M., and Liu, P.: Characteristics of secondary

850   circulations in the convective boundary layer over two-dimensional

851   heterogeneous surfaces. *J. Meteor. Res.*, **30**, 944-960,

852   https://doi.org/10.1007/s13351-016-6016-z, 2016.

853   Sommeria, G., and LeMone, M. A.: Direct testing of a three-dimensional model of the

854   planetary boundary layer against experimental data. *J. Atmos. Sci.,* **35**, 25-39,

855   https://doi.org/10.1175/1520-0469(1978)035<0025:DTOATD>2.0.CO;2, 1978.

856   Sullivan, P. P., Moeng, C., Stevens, B., Lenschow, D. H., and Mayor, S. D.: Structure

857   of the Entrainment Zone Capping the Convective Atmospheric Boundary Layer,

858   Journal of the Atmospheric Sciences, 55(19), 3042-3064.

https://doi.org/10.1175/1520-0469(1998)055<3042:SOTEZC>2.0.CO;2, 1998.

Tyagi, B., and Satyanarayana, A. N. V.: The Budget of Turbulent Kinetic Energy during Premonsoon Season over Kharagpur as Revealed by STORM Experimental Data. *ISRN Meteorology*, **2013**, 1-11, doi: 10.1155/2013/972942, 2013.

Wang, B. B., Ma, Y. M., Chen, X. L., Ma, W. Q., Su, Z. B., and Menenti, M.: Observation and simulation of lake–air heat and water transfer processes in a high-altitude shallow lake on the Tibetan Plateau [J]. J. Geophys. Res., 120(24): 12327-12344. doi:10.1002/2015JD023863, 2015.

Wang, C., Tian, W. S., Parker, D. J., Marsham, J. H. and Guo, Z.: Properties of a simulated convective boundary layer over inhomogeneous vegetation. *Quart. J. Roy. Meteor. Soc.*, **137**, 99-117, https://doi.org/10.1002/qj.724, 2011.

Wang, Y., Xu, X., Liu, H., et al., Wang, Y. J., Xu, X. D., Liu, H. Z., Li, Y. Q., Li, Y. H., Hu, Z. Y., Gao, X. Q., Ma, Y. M., Sun, J. H., Lenschow, D. H., Zhong, S. Y., Zhou, M. Y., Bian, X. D., and Zhao, P.: Analysis of land surface parameters and turbulence characteristics over the Tibetan Plateau and surrounding region. *J. Geophys. Res.: Atmospheres*, **121**, 9540-9560, doi:10.1002/2016JD025401, 2016.

Wen, L. J., Lyu, S. H., Li, Z. G., Zhao, L., and Nagabhatla, N.: Impacts of the Two Biggest Lakes on Local Temperature and Precipitation in the Yellow River Source Region of the Tibetan Plateau. *Adv. Meteor.*, **2015**, 10, doi:10.1155/2015/248031, 2015.

Wen, L. J., Lyu, S. H., Kirillin, G., Li, Z. G., and Zhao, L.: Air-lake boundary layer

and performance of a simple lake parameterization scheme over the Tibetan highlands, Tellus A: Dynamic Meteorology and Oceanography, 68:1, 31091. doi: 10.3402/tellusa.v68.31091, 2016.

Xu, Z. W., Ma, Y. F., Liu, S. M., Shi, W. J., Wang, J. M.: Assessment of the Energy balance closure under advective conditions and its impact using remote sensing data. Journal of Applied Meteorology and Climatology, 56(1). doi:10.1175/JAMC-D-16-0096.1, 2016.

Zhang, W. C., Guo, J. P., Miao, Y. C., Liu, H., Song, Y., Fang, Z., He, J., Lou, M. Y., Yan, Y., Li, Y., and Zhai, P. M.: On the summertime planetary boundary layer with different thermodynamic stability in China: A radiosonde perspective [J]. J. Climate, 31(4): 1451-1465. doi:10.1175/JCLI-D-17-0231.1, 2018.

Zhao, Y., Xu, X. D., Ruan, Z., Chen, B., and Wang, F.: Precursory strong-signal characteristics of the convective clouds of the Central Tibetan Plateau detected by radar echoes with respect to the evolutionary processes of an eastward-moving heavy rainstorm belt in the Yangtze River Basin. *Meteor. Atmos. Phys.,* 1-16, https://doi.org/10.1007/s00703-018-0597-2, 2018.

Zheng, D. H., Velde, R. V. D., Su, Z. B., Wang, X., Wen, J., Booij, M. J., Hoekstra, A. Y., and Chen, Y. Y.: Augmentations to the Noah Model Physics for Application to the Yellow River Source Area. Part II: Turbulent Heat Fluxes and Soil Heat Transport. *J. Hydromete.,* **16**, 2677-2694, https://doi.org/10.1175/JHM-D-14-0199.1, 2015.

Zhou, Y., Li. D., Liu, H. and Li, X.: Diurnal variations of the flux imbalance over

903   homogeneous and heterogeneous landscapes. Boundary-Layer Meteorology,

904   168:417–442. https://doi.org/10.1007/s10546-018-0358-2, 2018.